



N-doped carbon quantum dots/TiO₂ composite with improved photocatalytic activity

Natércia C.T. Martins^a, Joana Ângelo^a, Ana Violeta Girão^b, Tito Trindade^b,
Luísa Andrade^a, Adélio Mendes^{a,*}

^a LEPABE, Departamento de Engenharia Química, Faculdade de Engenharia, Universidade do Porto, Rua Dr. Roberto Frias, 4200-465 Porto, Portugal

^b Departamento de Química-CICECO, Universidade de Aveiro, Campus de Santiago, Aveiro, Portugal

ARTICLE INFO

Article history:

Received 29 January 2016

Received in revised form 5 April 2016

Accepted 8 April 2016

Available online 11 April 2016

Keywords:

N-doped carbon quantum dots

P25

Photocatalyst

NO photo-oxidation

Methylene blue degradation

ABSTRACT

A new composite of TiO₂ (P25) and N-doped carbon quantum dots (P25/NCQD) was prepared by a hydrothermal method and was used for the first time as catalyst of the photo-oxidation of NO under UV and visible light irradiation. P25/NCQD composite exhibited a NO conversion (27.0%) more than two times higher of that observed for P25 (10%) under visible light and the selectivity of the process was increased from 37.4% to 49.3%. The composite also showed better photocatalytic performance than P25 in the UV region with increases of 36.3% on NO conversion and 16.8% on selectivity. Moreover, compared with P25, the photodegradation ratio of methylene blue was enhanced from 68% to 91% after UV irradiation for 1 h. NCQD played a crucial role on the photocatalytic activity improvement of P25/NCQD, increasing visible light absorption, slowing the recombination and improving the charge transfer.

© 2016 The Authors. Published by Elsevier B.V. This is an open access article under the CC BY-NC-ND license (<http://creativecommons.org/licenses/by-nc-nd/4.0/>).

1. Introduction

Nitrogen oxides (NO_x) are well known air pollutants that cause severe environmental and health problems. Although NO_x (NO and NO₂) can be formed during natural processes such as lightning, the majority of the emissions are produced by anthropogenic activities mainly by coal power plants and road traffic [1,2]. Along with SO₂, NO_x is responsible for the formation of acid rain that causes corrosion of buildings and harms forests, crops and aquatic life [3]. High concentrations of NO_x in the atmosphere can also contribute to the formation of tropospheric ozone and photochemical smog that can lead to serious respiratory problems such as emphysemas and bronchitis [4,5]. Although stricter legislation has been adopted by the European Union members, NO_x levels in the atmosphere are still above the limit value recommended by the latest EU directive [6], particularly in urban areas [7]. On the other hand, water contamination with organic pollutants (e.g. dyes, herbicides, phenolic compounds) from industry, agriculture and other human activities are also a subject of serious concern [8]. The release of polluted wastewaters into the aquatic ecosystem represents both environmental and public health risks because of their negative ecotoxicological effects and bioaccumulation in aquatic life [9]. For

all the reasons discussed above, the development of new and efficient methods for NO_x and organic pollutants removal from the environment is of great importance.

In the last decade, photocatalytic oxidation using semiconductors as catalysts has become one of the most promising approaches for removing inorganic (e.g. NO_x) [10,11] and organic (e.g. dyes) [12] pollutants from gas or liquid phases. Among semiconductor photocatalysts, titanium dioxide (TiO₂) has received considerable attention due to its high photocatalytic activity, high chemical stability, low toxicity and low cost [13]. When TiO₂ is exposed to sunlight, photons with energy equal or higher than its bandgap energy are absorbed leading to the promotion of electrons (e⁻) from the valence to the conduction band and the consequent formation of positively charged vacancies (holes, h⁺) in the valence band. Both species migrate to the surface of the semiconductor where they participate in oxidation (h⁺) and reduction (e⁻) reactions forming high reactive radical species. Holes have a potential sufficiently positive to oxidize water molecules and OH⁻ adsorbed onto the semiconductor surface producing OH• radicals, which will then promote the oxidation of harmful pollutants like NO_x or organic dyes [14]. On the other hand, photoexcited electrons react with oxygen molecules to form superoxide anions O₂•⁻ that participate in the redox reactions involved in the degradation of the pollutants [3,11]. Recently, some authors reported that holes can also be trapped by TiO₂ surface lattice oxygen ions, either protonated (>OH_s⁻) or deprotonated (>O_s²⁻), to generate surface lattice radicals (-OH_s•/-O_s•⁻) that

* Corresponding author.

E-mail address: mendes@fe.up.pt (A. Mendes).

can than participate in several redox reactions that originate the degradation of pollutants [15].

Several materials incorporating photocatalytic TiO_2 have already been prepared for air and water purification applications, however, only very few were made commercially available [16–18]. Moreover, the results of NO_x photoabatement tests, using materials containing TiO_2 , under real outdoor conditions are still behind the expectations. This is mainly due to the fact that TiO_2 has one important drawback: its wide band gap (3.2 eV for anatase) requires photocatalytic activation by ultraviolet irradiation (about 4% of the solar spectrum), giving rise to very low solar photoconversion efficiencies. Therefore, for practical use, the development of photocatalysts activated by visible light is extremely important.

Many strategies have been adopted to extend TiO_2 photocatalytic activity into the visible region, including dye sensitization [19,20], noble metal deposition [21,22], doping with metal and non-metal elements [23,24] and coupling with narrow bandgap semiconductors [20,25]. In particular, the modification of TiO_2 with carbon nanomaterials is being increasingly investigated. TiO_2 /carbon composites have shown improved optical absorbance in the visible spectral range and enhanced charge separation efficiency, when compared with pristine TiO_2 [26,27]. Several types of carbon nanomaterials, such as, carbon nanotubes, fullerenes and graphene, have been used for the production of TiO_2 /carbon composites with promising photocatalytic activities in the visible region [28–30]. Recently, a new member of carbon family, carbon quantum dots (CQD), have attracted considerable attention due to their unique properties. Like traditional semiconductors, CQD show photoluminescence properties and in addition possess the advantages of low toxicity, water solubility and resistance to photobleaching [31]. As a result, they have been widely applied in many fields such as chemical sensing, bioimaging, electrocatalysis and photocatalysis [32]. In last years, N-doping of CQD has shown great potential for enhance the photocatalytic activity of TiO_2 /CQD composites. Zhang et al. [33] synthesized N-doped carbon quantum dots (NCQD) and combined it with rutile TiO_2 to form TiO_2 /NCQD composites which exhibited enhanced visible-light photocatalytic activity towards the degradation of rhodamine B when compared with N-free TiO_2 /CQD composites. These authors have reported that N-doping lowers the work function of CQD, which is probably the main reason for the enhanced photocatalytic activity of the TiO_2 /NCQD.

To the best of our knowledge there are no reports in the literature concerning the use of TiO_2 /NCQD composites in the photocatalytic removal of NO_x . Moreover, studies of the oxidation of NO_x using photocatalysts with visible light activity are still scarce. In this work NCQD were prepared by microwave-assisted method and then hydrothermally combined with P25 TiO_2 to obtain a new composite, P25/NCQD. The composite was used as catalysts of the photo-oxidation of NO under UV and visible light and was also tested in the photodegradation of methylene blue (MB) under UV light. In both cases the composite showed higher photocatalytic activity than commercial P25 TiO_2 . The reasons for the enhanced photocatalytic activity of P25/NCQD have been discussed based on the experimental results and on recent literature.

2. Materials and methods

2.1. Materials

Glycerol (ASC reagent $\geq 99.5\%$), ammonium phosphate dibasic (ASC reagent $\geq 98\%$) and 4,7,10-trioxa-1,13-tridecanediamine (TTDDA, 97%) were purchased from Aldrich and used as received. Aeroxide® TiO_2 P25 was obtained from Evonik Industries. Dialysis

was done using Spectra/Por Float-A-Lyzer G2 dialysis tubes (MWCO 500–1000 au).

2.2. Synthesis of N-doped carbon quantum dots (NCQD)

NCQD were synthesized using an adaptation of the method reported by Lui et al. [34]. 5 g of glycerol were mixed with 2 mL of ammonium phosphate solution (20 mM). Then 1 mL of TTDDA was added under vigorous stirring. The solution was put in the ultrasounds during 3 min and then it was transferred to a domestic microwave oven and heated during 7 min at 700 W. After cooling down to room temperature the resultant dark red solution was diluted with 20 mL of water and dialyzed against pure water during 3 days. Upon completion of the purification process by dialysis, the yellow solution obtained was lyophilized to collect NCQD.

2.3. Preparation of P25/NCQD composite

P25/NCQD composite was produced by a hydrothermal method. 1 g of P25 was dispersed in a solution of distilled water (40 mL) and ethanol (20 mL). The suspension was stirred for five minutes and then 2.5 mL of an aqueous NCQD solution (4 mg/L) was added. The mixture was kept stirring for 5 h and then was transferred into a 125 mL Teflon-sealed autoclave and maintained at 130 °C for 4 h. Finally, the resulting composite was recovered by centrifugation (15 min at 5000 rpm), washed with distilled water two times and dried at 60 °C during 24 h.

2.4. Materials characterization

Morphological, structural and analytical characterization of the obtained NCQD and P25/NCQD composite was performed by Electron Microscopy. Bright-Field Transmission Electron Microscopy (BF-TEM) and High-Resolution (HR) TEM images were obtained using a JEOL 2200FS electron microscope equipped with Oxford Energy Dispersive X-rays (EDX) detector and in-column Omega filter, operated at 200 kV. A drop of the obtained samples was highly diluted in ultra-pure water and then placed onto the surface of an Agar Scientific copper grid with a holey amorphous carbon film and left to dry in air. After being completely dried, all the samples were immediately kept in a vacuum box till being used for examination under the TEM microscope. Observation, acquisition and imaging analysis were carried out using Gatan Digital Micrograph Software 1.84.1282 (Gatan Inc.® 1996–2010). Scanning-TEM EDX mapping was performed using INCA Energy Software (Oxford Instruments Analytical® 2006–2011). Fourier transform infrared (FTIR) spectra were recorded on a BOMEM (model MB154) spectrophotometer scanning from 4000 to 500 cm^{-1} . Zeta potential measurements were performed using a Zeta Sizer Nano Series (Malvern) equipment. X-ray photoelectron spectroscopy (XPS) was obtained using a KRATOS axis ultra HAS-Vision X-ray photoelectron spectrometer with a monochromatic X-ray source (Al). Thermogravimetric analysis (TGA) curves of the samples were obtained by a TG 209 F1 Iris Thermal-microbalance (Netzsch) in nitrogen atmosphere using an input flow rate of 30 mL min^{-1} and a heating ramp of 3 °C min^{-1} up to 600 °C. Diffuse reflectance spectra of the powder samples were recorded on a Shimadzu UV-3600 UV-vis-NIR spectrophotometer, equipped with a 150 mm integrating sphere and using BaSO_4 as 100% reflectance standard. The specific surface area of the catalysts was measured at 77 K on a Quanta Chrome Nova-1200 (USA) equipment using Brunauer-Emmett-Teller nitrogen adsorption-desorption method (BET). Before being analysed, the samples were treated at 150 °C for 2 h under vacuum to remove any surface-adsorbed species. Powder X-rays Diffraction (XRD) patterns of the prepared samples were recorded on a Phillips Empyrean diffractometer system operated at 45 kV/40 mA in continuous mode, with

a step size of 0.0130 and scan step time of 2698.92 s, controlled by the PANalytical X'Pert HighScore software. The basic lattice parameters were obtained using Checkcell, a modified version of Celref free software (<http://www.inpg.fr/LMGP>). Electrochemical impedance spectroscopy (EIS) measurements were performed with a ZENNIUM workstation, with a frequency range between 100 mHz and 100 kHz and the magnitude of the modulation signal was 10 mV. All measurements were performed at room temperature and open-circuit voltage. Prepared thin films (active area of ca. 0.238 cm²) applied on the FTO coated substrates were used as working electrodes, 99.9% platinum wire was used as counter-electrode (Alfa Aesar, Germany) and Ag/AgCl/sat. KCl was used as reference electrode (Metrohm, Switzerland). The measurements were conducted using an aqueous solution of H₂SO₄ 0.5 M as electrolyte (pH = 0.8).

2.5. Photocatalytic activity tests

2.5.1. NO photo-oxidation

The experimental setup used in NO photo-oxidation tests consists of four main sections: (i) feed, (ii) reactor, (iii) NO_x quantification and (iv) computer monitoring/control. In the first section, the gas stream with the desired NO concentration, relative humidity and flow rate, is prepared and fed to the photoreactor. The reaction section is composed by a photoreactor (with a Pyrex® window) designed to hold the samples, minimizing dead and stagnant volumes. A lamp with the desired wavelength is placed above the reactor. NO and NO₂ concentrations are quantified using a chemiluminescence analyser (ThermoElectron 42C). A computer controls the experimental setup and acquires the relevant data. The reactor is placed inside a thermostatic cabin to ensure controlled and constant temperature. Detailed information about the setup used can be found elsewhere [11].

Samples were tested as powder films (5 × 5 cm²) obtained pouring the powder evenly over an aluminum slab and then pressing at 5 bar for 5 min. This procedure yielded homogeneous powder films ca. 0.5 mm thick. Photocatalytic tests were performed at 25 °C with a feed rate of 0.7 L min⁻¹ of NO at 1 ppm_v in air and 50% of relative humidity. As source of UV light an ultraviolet lamp (UV-A, highest emission at 365 nm) with two 6 W black-light-blue bulbs (VL-206-BLB, Vilbert Lourmat, France) was employed. The visible light tests were conducted with a regular fluorescent lamp (Philips Master TL-Mini Super 80 6 W/840) equipped with a filter to obtain light of λ > 400 nm. The irradiance at the catalyst surface, estimated with a radiometer, was 10 W m⁻² and 50 W m⁻² for the UV and visible light tests, respectively.

In the operating conditions used in this work, the products resulting from the photo-oxidation of NO are nitrite (NO₂⁻), nitrate (NO₃⁻) and NO₂ [11]. Since NO₂ is even more harmful than NO to human health and to the environment, the desired reaction products are the ionic species. Therefore, two parameters were used to evaluate the performance of the prepared photocatalysts, NO conversion (Eq. (1)) and selectivity towards the formation of ionic species (Eq. (2)):

$$\text{Conversion} = \left(\frac{C_{\text{NO}}^{\text{in}} - C_{\text{NO}}^{\text{out}}}{C_{\text{NO}}^{\text{in}}} \right) \times 100 \quad (1)$$

$$\text{Selectivity} = \left(1 - \frac{C_{\text{NO}_2}^{\text{out}}}{C_{\text{NO}}^{\text{in}} - C_{\text{NO}}^{\text{out}}} \right) \times 100 \quad (2)$$

where C_{NO} and C_{NO₂} stand for the concentration of NO and NO₂, respectively, and the superscripts (in and out) refer to the reactor's inlet and outlet streams. The photo-oxidation of NO was followed during 85 h under UV radiation and 120 h under visible radiation.

2.5.2. Methylene blue degradation

Photocatalytic degradation of methylene blue (MB) dye was performed in a 250 mL cylindrical glass vessel containing 100 mL of MB solution (0.01 g/L) and 50 mg of the photocatalyst. The mixture was firstly stirred during 30 min in the dark to ensure the establishment of an adsorption-desorption equilibrium. After that, the photoreactor vessel was irradiated with UV light produced by an ultraviolet lamp (UV-A, highest emission at 365 nm) with two 6 W black-light-blue bulbs (VL-206-BLB, Vilbert Lourmat, France) positioned 10 cm above the surface of reaction solution (irradiance at the surface of the mixture of 10 W/m²). Aliquots of 3 mL were collected every 30 min in a period of 4 h, then were centrifuged and the supernatant was analysed in a UV-vis spectrophotometer (Shimadzu UV-3600 UV-vis-NIR spectrophotometer) to record the absorption band maximum (665 nm) of MB as a function of the time; the concentration of MB (C) is proportional to the maximum absorbance at 665 nm (A). Thereby, the MB change of concentration (C/C₀) was obtained from the absorbance history (A/A₀), where C₀ is the concentration after adsorption-desorption equilibrium and A₀ is the correspondent absorbance. All experiments were repeated three times and the average computed.

3. Results and discussion

3.1. Characterization of N-doped carbon quantum dots

Although NCQD were prepared using an adaptation of a method reported on the literature [34], in the conditions employed in this research, particles with different characteristics were obtained (e.g. size and crystallinity) and new features were found. BF-TEM analysis revealed that the as prepared NCQD present a quasi-spherical morphology with diameters ranging from 6 to 13 nm and mean of 9.4 nm (Fig. 1A). HR-TEM imaging of our samples demonstrated that in this case most of the NCQD are nanocrystalline with well-resolved lattice fringes, which differs from the findings reported by Liu et al. [34]. Fig. 1B shows a representative HR-TEM image of NCQD in which the interplanar distances 2.096 and 2.029 Å correspond respectively to the (010) and (011) lattice planes of the hexagonal graphitic carbon (ICDD reference code 01-075-1621). The powder XRD patterns for the NCQD samples (Fig. S1, Supporting Information) are in good agreement with the HR-TEM results shown above, thus showing the crystalline graphitic carbon structure. Although the broad peak centred about 20° (2θ) may suggest the presence of amorphous NCQD, there was no evidence for this type of carbon by HR-TEM. Therefore the broadening of such diffraction peak might be related to the nanometer size of the particles. The few relatively sharp peaks around 2.9–2.3 Å might be indicative also of microcrystallites present in the carbon samples. Although not detected by HR-TEM, these diffraction peaks can be attributed to another crystalline hexagonal carbon phase (ICDD reference code 00-026-1081) that could be formed during the NCQD synthesis [35,36].

The FTIR spectrum of NCQD (Fig. S2, Supporting Information) displays characteristic vibrational bands at 3380 cm⁻¹ (O–H and N–H stretching), 2922 and 2868 cm⁻¹ (CH₂, C–H antisymmetric and symmetric stretching), 1645 cm⁻¹ (C=O stretch in amide and carboxylic groups), 1568 cm⁻¹ (N–H deformation in amides), 1455 cm⁻¹ (OH in plane bending in carboxylic groups) and 1118 cm⁻¹ (C–O stretch). Most of the non passivated CQD samples described in the literature present a negative zeta potential due to the presence of abundant carboxylic groups on their surface [37,38]. The NCQD prepared in this work show in opposition a positive zeta potential (13.6 ± 3.37 mV, pH = 7.6). This means that conversion of the carboxylic groups, that have been formed during the pyrolysis of glycerol, into amide groups, occurred in large exten-

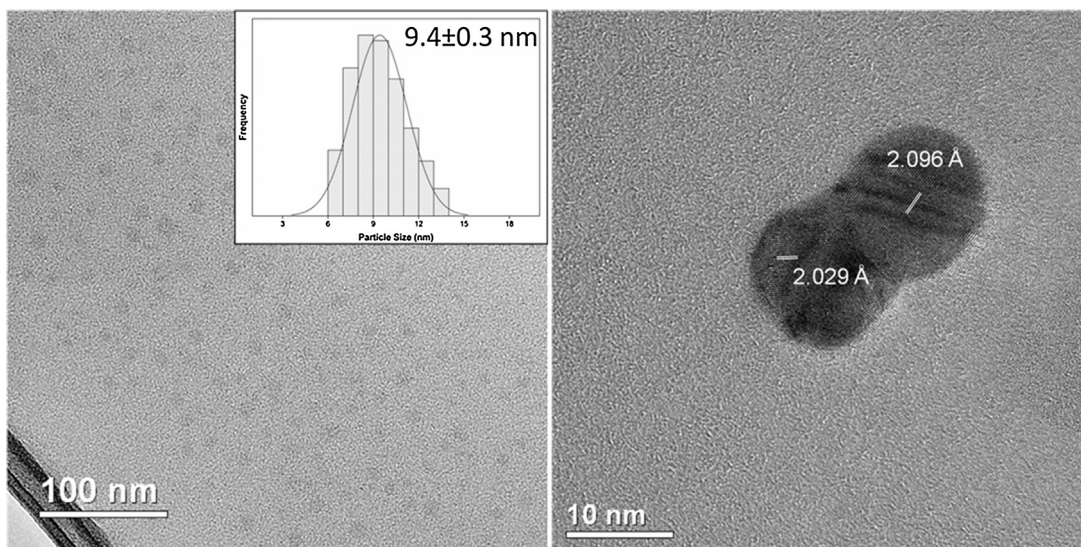


Fig. 1. (A) BF-TEM image of NCQD and histogram for the particle size distribution; (B) HR-TEM image of NCQD.

sion after passivation with TTDDA. The strong band at 1568 cm^{-1} in the FTIR spectrum confirms this hypothesis. The positive zeta potential of NCQD colloid also suggests the presence of protonated amine groups on the surface of the particles when dispersed in water ($\text{pH} < 7$) [39,40].

The chemical composition of the NCQD was further characterized by X-ray photoelectron spectroscopy (XPS). The XPS survey spectrum (Fig. S3, Supporting Information) shows that the NCQD are mainly composed of carbon (75.3%), oxygen (17.2%) and nitrogen (7.61%). Lui et al. [34] have synthesized surface passivated carbon quantum dots by microwave pyrolysis of glycerol in the presence of TTDDA. We have used a similar route to synthesize the carbon quantum dots however we found by XPS analysis that these particles were not only surface passivated with amide/amine groups, but also the carbon cores were doped with nitrogen. In fact, the deconvoluted high resolution N 1s spectrum of NCQD (Fig. 2B) reveals the presence of three peaks at 398.9, 400.1 and 401.4 eV, which are attributed to different types of nitrogen: amide/amine, pyrrolic and graphitic, respectively [41,42]. This means that TTDDA acts not only as passivation agent but also as precursor for N-doping. Zhai et al. [42] have also reported the production of N-doped surface passivated CQD by microwave assisted pyrolysis of citric acid in the presence of a primary amine (1,2-ethylenediamine). The deconvoluted high resolution C 1s spectrum of the NCQD (Fig. 2A) shows four main peaks at 284.7, 285.7, 286.0, and 287.3 eV attributed to C–C/C=C, C–N, C–O and C=O respectively [43]. From all the characterization done it was possible to conclude that the surface of the NCQD is functionalized with different organic groups such as amide, amine, hydroxyl and carboxyl. In addition the carbon cores are doped with N.

3.2. Characterization of P25/NCQD composite

A new composite (P25/NCQD) of P25 decorated with N-doped carbon quantum dots was prepared using a hydrothermal method. TEM images clearly illustrate the successful coupling of NCQD onto P25 and, in the final composite, smaller spherical particles of NCQD intermixed with larger crystalline nanoparticles of P25 (TiO_2 mixture of 80% anatase and 20% rutile) are easily spotted, as shown in Fig. 3A. The HR-TEM image in Fig. 3B shows the lattice spacing of 2.016 Å for the (101) diffraction plane of the crystalline NCQD. Other well resolved interlayer distances were also identified for the (200) crystalline plane of anatase (1.872 Å) and for the (111) plane

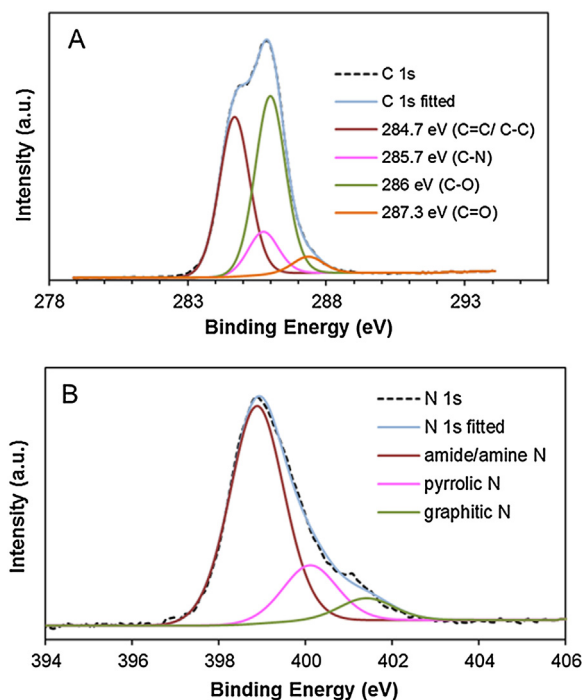


Fig. 2. High resolution XPS spectra of NCQD: (A) C1s and (B) N1s.

of rutile (2.184 Å). STEM-EDX elemental mapping of P25/NCQD was also carried out (Fig. S4, Supporting Information). The images obtained clearly show areas where Ti and O are absent suggesting the presence of NCQD in these areas. XRD pattern of the P25/NCQD shows sharp and intense reflections attributed to anatase and rutile TiO_2 polymorphs confirming the presence of P25 (Fig. S1, Supporting Information). However, the typical XRD reflections for carbon were not observed in the P25/NCQD sample due to their very low content in the final material and also low crystallinity when compared to that of P25.

Fig. 4 shows TGA curves of P25 and of P25/NCQD composite. The weight loss before 120°C of both P25 and the composite is attributed to the elimination of adsorbed water and is not shown in Fig. 4. The 0.36% weight loss observed between 120°C and 250°C for P25 and P25/NCQD should result from dehydroxylation of sur-

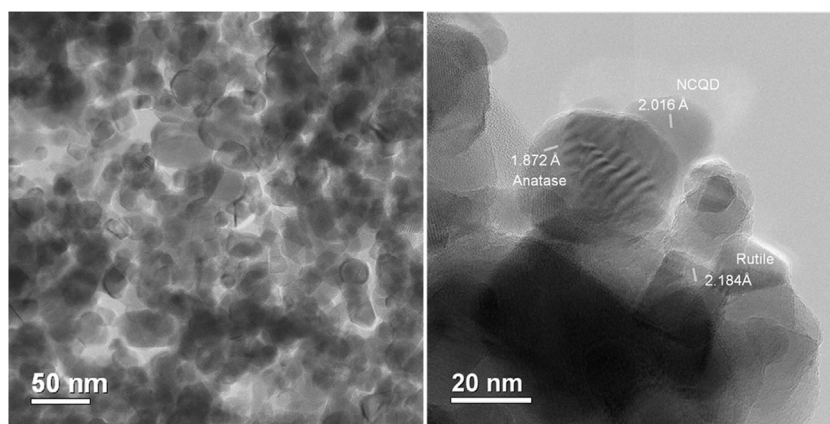


Fig. 3. (A) BF-TEM image of P25/NCQD; (B) HR-TEM image of P25/NCQD showing the lattice fringes of both P25 (Anatase and Rutile polymorphs) and NCQD.

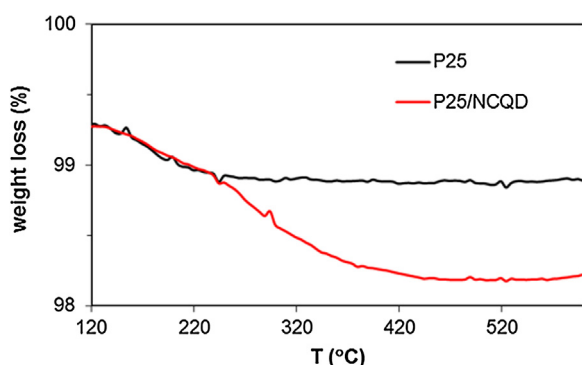


Fig. 4. TGA curves of P25 and of P25/NCQD composite.

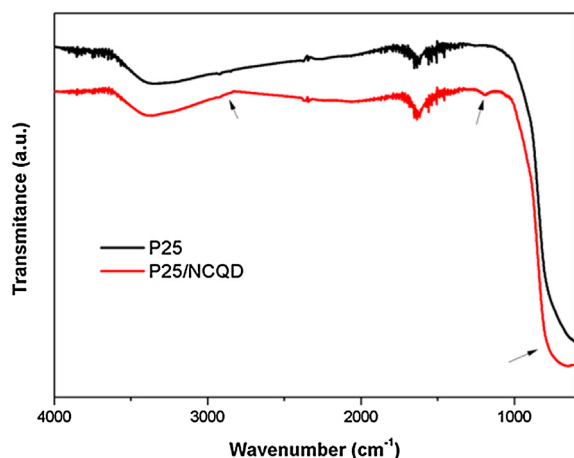


Fig. 5. FTIR spectra of P25 and of P25/NCQD samples. The arrows highlight the main differences between the two spectra.

face attached water and OH groups [44,45]. For the composite, a third weight loss of 0.69% is observed between 250 °C and 520 °C corresponding to the slow combustion of NCQD. This means that the content of the NCQD on the composite is about 0.69%.

FTIR analyses were performed in order to investigate the interaction between P25 and NCQD (Fig. 5). P25 spectrum displays three characteristic peaks at 3370, 1630 and 650 cm^{-1} associated with stretching vibrations of hydrogen-bonded water molecules and hydroxyl groups, bending vibrations of O–H group and Ti–O–Ti bridging stretching mode respectively [46,47]. In the FTIR spectrum of P25/NCQD three new features appeared. A small shoulder at 2900 cm^{-1} is assigned to C–H stretching in NCQD and a peak

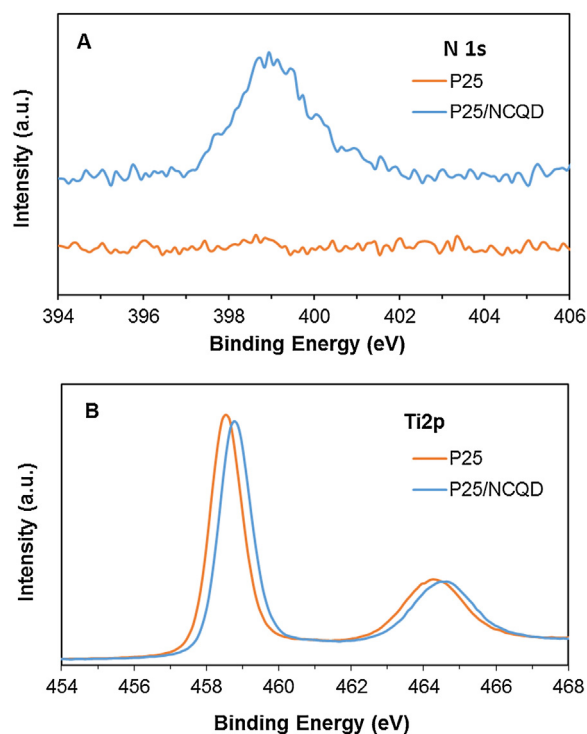


Fig. 6. XPS high resolution spectra of P25 and of P25/NCQD samples. (A) N1s and (B) Ti2p.

at 1170 cm^{-1} is associated with C–O stretching vibration. It was also observed that the broad absorption below 1000 cm^{-1} became wider and shifted toward high wavenumber when compared to that of P25. This behaviour was associated by several authors [28,48] to a combination of Ti–O–Ti and Ti–O–C vibrations and suggests that the coupling between P25 and NCQD is achieved by the formation of the Ti–O–C bond.

The presence of nitrogen was detected by XPS in P25/NCQD and not in P25 sample (Fig. 6A). This confirms that the NCQD are present in the P25/NCQD composite. The Ti 2p high resolution spectra for P25/NCQD and P25 are shown in Fig. 6B. For P25/NCQD the binding energies of Ti2p_{3/2} and Ti2p_{1/2} are positioned at 458.8 and 464.7 eV, respectively. Compared to P25, the Ti2p peaks of P25/NCQD are shifted towards a higher binding energy. The shift of 0.3–0.5 eV suggests that the chemical environment of Ti in the composites changed due to strong interaction between P25 and NCQD with formation of Ti–O–C bonds [45,48].

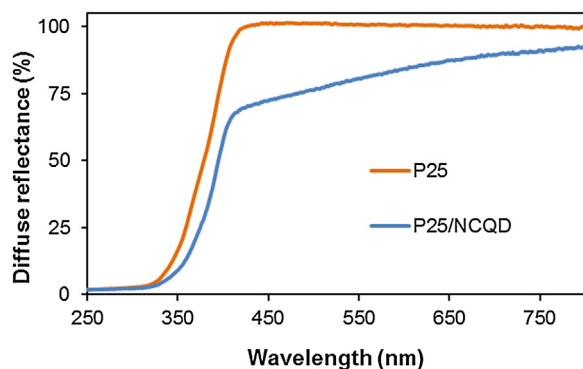


Fig. 7. Diffuse reflectance spectra of P25 and P25/NCQD.

The diffuse reflectance spectra of P25 and P25/NCQD composite are shown in Fig. 7. P25 exhibits a reflectance of 100% above 425 nm, while the composite shows a considerable decrease of the reflectance in the range of 425–800 nm. At 425 nm the reflectance is 69.8% for P25/NCQD. This means that the composites present significant absorption in the visible region. The bandgaps of the two compounds were estimated from diffuse reflectance spectra following a method based on Tauc equation and described elsewhere [49]. For P25 two bandgaps were found at 3.15 and 3.05 eV corresponding to the two crystalline forms of TiO₂, anatase and rutile, respectively. P25/NCQD showed a bandgap of 2.95 eV. The slight decrease of the bandgap of the composite when compared with P25 may be attributed to chemical bonding between P25 and NCQD with the formation of Ti–O–C bond [28,50]. Therefore, NCQD have an important role in the enhancement of visible light absorption in the P25/NCQD composite, which is expected to improve its photocatalytic activity under visible light irradiation.

3.3. Photocatalytic activity of P25/NCQD composite

3.3.1. NO photo-oxidation

P25/NCQD was tested as catalysts of the photo-oxidation of NO under UV and visible light. After 85 h of UV light irradiation, the composite P25/NCQD showed a NO conversion of 79.6% and a selectivity of 47.9% (Fig. 8A and B). These values were much higher than those obtained for P25 (58.4% of NO conversion and 41.0% of selectivity). Therefore, compared with P25, the composite shows a 36.3% increase on NO conversion and a 16.8% increase on selectivity. Moreover, after reaching steady-state the photocatalysts showed good stability for at least 48 h.

When submitted to visible light, P25/NCQD also showed superior photocatalytic activity compared with P25 during at least 120 h (Fig. 9A and B). While in the presence of P25 a conversion of 10% at steady state was obtained, with P25/NCQD the achieved conversion was 27%. This means that the conversion increases 2.7 times when using P25/NCQD as photocatalyst. The selectivity of the photocatalytic process is also considerably higher when using the composite (49.3%) compared with P25 (37.4%).

To the best of our knowledge P25/NCQD synthesized in this work is the first example of a composite of TiO₂ and carbon quantum dots with photocatalytic activity towards NO degradation under visible light ($\lambda > 400$ nm). P25/NCQD composite showed a better photocatalytic performance than N-doped TiO₂ particles prepared by several researchers [46,51,52].

To check if the enhancement of the photocatalytic activity of the P25/NCQD composite is only related to the presence of the NCQD or if it is also connected with the hydrothermal treatment suffered by the powders, the photoactivity of P25 hydrothermally treated at 130 °C during 4 h (P25-HT) was also tested. As shown in Fig. S5 (see Supporting Information), P25-HT present a higher NO con-

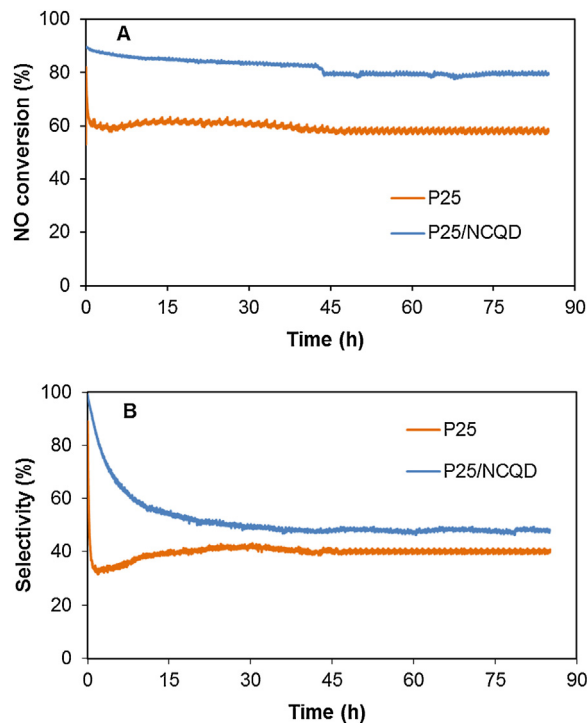


Fig. 8. NO conversion (A) and selectivity (B) for P25, P25/NCQD composite during 85 h under UV radiation.

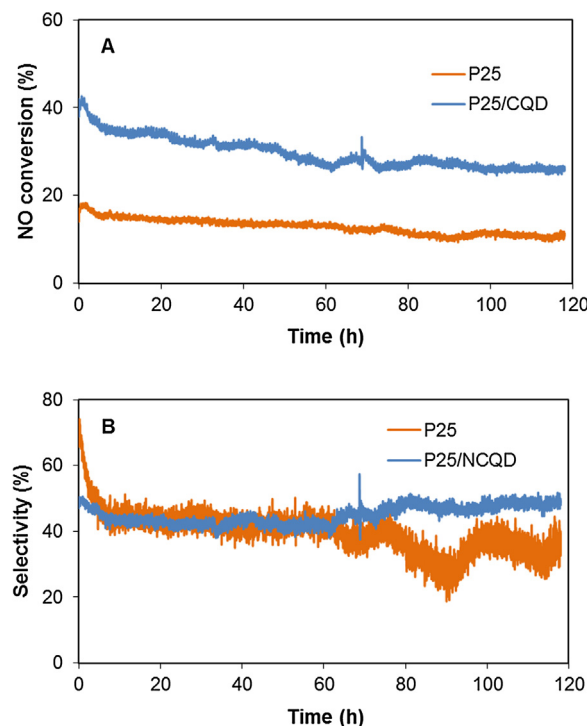


Fig. 9. NO conversion (A) and selectivity (B) for P25, P25/NCQD composite during 120 h under visible light irradiation.

version than untreated P25 both under UV and visible irradiation suggesting that the hydrothermal treatment contributes partially to the enhancement of the catalysts photoactivity. This behaviour could be attributed to the formation of more hydroxyl groups in the TiO₂ surface. According to Yu et al. [53], more hydroxyl groups

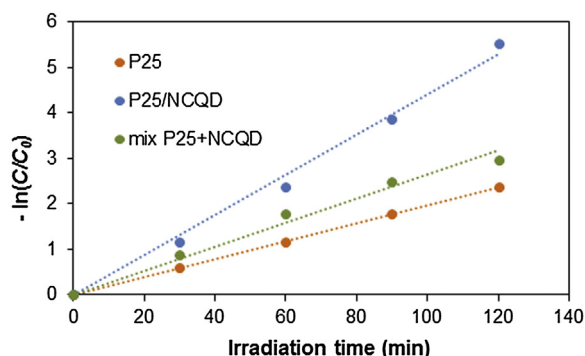


Fig. 10. Plots of $-\ln(C/C_0)$ versus t for the photodegradation of MB by P25, P25/NCQD and mix P25 + NCQD.

can generate more hydroxyl radicals, enhance the adsorption of O_2 molecules and reduce recombination of photogenerated electrons and holes. It should be highlighted that a physical mixture (without hydrothermal treatment) of P25 and NCQD (mix P25 + NCQD) showed significantly lower photocatalytic activity than P25/NCQD (Fig. S5, Supporting Information). This confirms that the hydrothermal treatment has a role on the enhancement of the photocatalytic activity not only fostering the formation of hydroxyl groups but also promoting a more efficient attachment of the NCQD to TiO_2 surface.

3.3.2. Photocatalytic activity in aqueous medium

The photocatalytic activity of P25 and P25/NCQD composite in aqueous medium, under UV irradiation, was assessed using methylene blue (MB). As shown in Fig. S6 (see Supporting Information), P25/NCQD composite presents a considerably higher photocatalytic activity towards MB degradation as compared with commercial P25. After 1 h of UV irradiation 91% of MB was photodegraded by P25/NCQD whereas only 68% of the initial dye was decomposed by P25. Moreover, the photocatalytic activity of P25/NCQD composite is higher than that of a physical mixture of P25 and NCQD (mix P25 + NCQD) showing that hydrothermal treatment promotes a more efficient attachment of the NCQD to TiO_2 surface. The decay of MB during the initial period (120 min) of UV excitation was fitted to a pseudo-first-order kinetics: $-\ln(C/C_0) = kt$, where k is the rate constant and t the irradiation time. Fig. 10 plots $-\ln(C/C_0)$ history for all photocatalysts. From this plot it was possible to estimate the rate constants for the MB degradation in the presence of these catalysts. Values of 0.019, 0.026 and 0.044 min^{-1} were obtained for P25, mix P25 + NCQD and P25/NCQD respectively. This means that the photocatalytic degradation rates of MB over P25/NCQD are 2.32 higher than that over P25. Similar MB photocatalytic degradation rates were found by other researchers when using TiO_2 /carbon composites as catalysts under UV light however, in the majority of the cases with larger concentrations of carbon (>1 wt.%) than that used in this work (0.69 wt.%) [27]. Tests of the photocatalytic performance of P25/NCQD composites were not implemented under visible light since there are reports that state that MB can suffer self-photosensitized degradation over TiO_2 when irradiated with visible light and thus would represent a non-photocatalytic contribution to the overall degradation of the dye [54].

3.4. Discussion on the enhanced photocatalytic activity of P25/NCQD composite

The performance of a photocatalyst can be determined by several factors such as specific surface area, crystallinity, light absorption range and efficiency of charge separation and trans-

port [28,55]. Generally, photocatalysts with larger specific surface area exhibit higher photocatalytic activity because a larger surface area provides more active sites for the adsorption of reactant molecules. The specific surface area of the P25 and P25/NCQD composite was measured using Brunauer-Emmett-Teller nitrogen adsorption-desorption method (BET) and values of 54.9 and $53.8 \text{ m}^2 \text{ g}^{-1}$, respectively, were obtained. This means that the higher photocatalytic activity of P25/NCQD is not related to a surface area enhancement. The similarity between the XRD patterns of P25 and P25/NCQD (Fig. S1, Supporting Information) reveals that crystallinity, crystal size and modifications on the crystal structure of TiO_2 are also not responsible for the differences between the photocatalytic activity of the two compounds.

The experimental results proved that hydrothermal treatment can impart higher photoactivity to TiO_2 . However, the presence of NCQD is necessary to achieve the highest NO degradation rates (Fig. S5, Supporting Information). Therefore NCQD have a key role on the enhancement of photocatalytic activity.

P25/NCQD displays enhanced visible light absorption (Fig. 7) and narrowing of the bandgap (from 3.05 eV to 2.95 eV) when compared with P25. Carbon doping is not expected to occur since usually C-doped TiO_2 is synthesized at temperatures higher than 600°C [50]. This leads us to conclude that the slight decrease of the bandgap could be related with chemical bonding between P25 and NCQD with formation of $Ti-O-C$ bond. In fact, FTIR and XPS results seem to support this hypothesis. Moreover, several authors reported that the presence of $Ti-O-C$ bond in TiO_2 /carbon composites favours charge transfer and can effectively extend light absorption to longer wavelengths [28,50]. On the other hand, NCQD can act as electron acceptor to trap the electrons from P25 conduction band and thus hinder electron-hole recombination leaving more charge carriers to form reactive species (e.g. OH^\bullet and $O_2^{\bullet-}$) that can promote the degradation of pollutants [48,56].

In a photocatalytic process the fast transport of charge carriers is important to prevent recombination. In order to study the charge transfer process on P25 and P25/NCQD the electrochemical impedance spectra of the two photocatalysts were measured. Comparing the Nyquist plots for P25 and P25/NCQD (Fig. S7, Supporting Information), it was observed that the diameter of the semicircle at high frequencies is smaller for P25/NCQD, which indicates a decrease in the charge transfer resistance on the surface [28]. This suggests that on P25/NCQD composite the transport of charge carriers is faster, contributing to a better separation of the photo-generated electron-hole pairs and consequently to a decrease of the recombination.

In summary, NCQD contribute to the enhanced photocatalytic activity of P25/NCQD composite in three ways: extending the light absorption into the visible range, slowing the recombination and improving the charge transfer.

4. Conclusions

A new photocatalyst (P25/NCQD) of P25 decorated with N-doped carbon quantum dots was prepared using a hydrothermal method. The P25/NCQD composite showed enhanced photocatalytic performance for NO photo-oxidation when compared with P25, both under UV and visible light. NO conversion increased from 10% to 27% and from 58.4% to 79.6% under visible and UV irradiation, respectively. Moreover, the selectivity of the process increased from 37.4% to 49.3% and from 41.0% to 47.9% under visible and UV irradiation, respectively. The photocatalytic activity of P25/NCQD in aqueous medium was also assessed using methylene blue (MB). Under UV radiation the MB degradation rate was 2.32 higher than the obtained for P25.

Although the hydrothermal treatment contributed to the enhanced photocatalytic activity of P25/NCQD, the main role on the photocatalytic performance of these nanocomposites was assigned to NCQD. These nanoparticles can strongly interact with TiO₂ extending the response of the composite to visible light. NCQD, in the P25/NCQD photocatalyst, can also act as efficient electron acceptors and transporters, slowing the recombination rate and consequently increasing photocatalytic activity.

Acknowledgments

Luísa Andrade and Natércia Martins acknowledge the European Research Council for funding within project BI-DSC—Building Integrated Dye sensitized Solar Cells (Contract Number: 321315). This work was also supported by research project SolarConcept (PTDC/EQU-EQU/120064/2010), co-financed by the European Union and the Portuguese Government through the Portuguese Foundation for Science and Technology (FCT), in the framework of the QREN Initiative and the European Regional Development Fund through the Operational Program for Competitiveness Factors. Ana Girão and Tito Trindade thank the project CICECO-Aveiro Institute of Materials (Ref. FCT UID/CTM/50011/2013), financed by national funds through the FCT/MEC and when appropriate co-financed by FEDER under the PT2020 Partnership Agreement. Joana Ângelo is grateful to the Portuguese Foundation for Science and Technology (FCT) for her Ph.D grant (SFRH/BD/79974/2011). Ana Girão thanks FCT for funding her Postdoctoral Research Grant (SFRH/BPD/66407/2009) and acknowledges Dr. Nuno João for XRD acquisition. The authors are thankful to CEMUP for the XPS analysis.

Appendix A. Supplementary data

Supplementary data associated with this article can be found, in the online version, at <http://dx.doi.org/10.1016/j.apcatb.2016.04.016>.

References

- [1] K. Skalska, J.S. Miller, S. Ledakowicz, *Sci. Total Environ.* 408 (2010) 3976–3989.
- [2] S. Roy, M.S. Hegde, G. Madras, *Appl. Energy* 86 (2009) 2283–2297.
- [3] S. Devahasdin, C. Fan Jr., K. Li, D.H. Chen, *J. Photochem. Photobiol. A* 156 (2003) 161–170.
- [4] B. Chen, C. Hong, H. Kan, *Toxicology* 198 (2004) 291–300.
- [5] S.A. Cormier, S. Lomnicki, W. Backes, B. Dellinger, *Environ. Health Persp.* 114 (2006) 810–817.
- [6] Directive 2008/50/EC on ambient air quality and cleaner air for Europe.
- [7] M.L. Williams, D.C. Carslaw, *Atmos. Environ.* 45 (2011) 3911–3912.
- [8] D. Shahidi, R. Roy, A. Azzouz, *Appl. Catal. B-Environ.* 174 (2015) 277–292.
- [9] X.Y. Liu, B.Y. Wang, Z.X. Su, *Desalination Water Treat.* 57 (2016) 1671–1683.
- [10] S. Chin, E. Park, M. Kim, J. Jeong, G.-N. Bae, *J. Jurng, Powder Technol.* 206 (2011) 306–311.
- [11] C. Águia, J. Ângelo, L.M. Madeira, A. Mendes, *J. Environ. Manag.* 92 (2011) 1724–1732.
- [12] M. Amin, J. Tomko, J.J. Naddeo, R. Jimenez, D.M. Bubb, M. Steiner, J. Fitz-Gerald, S.M. O'Malley, *Appl. Surf. Sci.* 348 (2015) 30–37.
- [13] K. Nakata, A. Fujishima, *J. Photochem. Photobiol. C* 13 (2012) 169–189.
- [14] A. Folli, S.B. Campbell, J.A. Anderson, D.E. Macphee, *J. Photochem. Photobiol. A* 220 (2011) 85–93.
- [15] J.F. Montoya, I. Ivanova, R. Dillert, D.W. Bahnemann, P. Salvador, J. Peral, *J. Phys. Chem. Lett.* 4 (2013) 1415–1422.
- [16] C.S. Poon, E. Cheung, *Constr. Build. Mater.* 21 (2007) 1746–1753.
- [17] M.M. Ballari, M. Hunger, G. Hüsken, H.J.H. Brouwers, *Appl. Catal. B-Environ.* 95 (2010) 245–254.
- [18] Keim Mineral Paints website, <http://www.keimpaints.co.uk> (accessed December 2015).
- [19] A.L. Stroyuk, A.I. Kryukov, S.Y. Kuchmii, V.D. Pokhodenko, *Theor. Exp. Chem.* 45 (2009) 209–233.
- [20] D.Y.C. Leung, X.L. Fu, C.F. Wang, M. Ni, M.K.H. Leung, X.X. Wang, X.Z. Fu, *Chemosuschem* 3 (2010) 681–694.
- [21] Z.K. Zheng, B.B. Huang, X.Y. Qin, X.Y. Zhang, Y. Dai, M.H. Whangbo, *J. Mater. Chem.* 21 (2011) 9079–9087.
- [22] S. Sakthivel, M.V. Shankar, M. Palanichamy, B. Arabindoo, D.W. Bahnemann, V. Murugesan, *Water Res.* 38 (2004) 3001–3008.
- [23] Z. Xu, J. Yu, *Nanoscale* 3 (2011) 3138–3144.
- [24] J. Yu, Q. Li, S. Liu, M. Jaroniec, *Chem. Eur. J.* 19 (2013) 2433–2441.
- [25] Y. Wang, Q. Wang, X. Zhan, F. Wang, M. Safdar, J. He, *Nanoscale* 5 (2013) 8326–8339.
- [26] R. Leary, A. Westwood, *Carbon* 49 (2011) 741–772.
- [27] K.R. Reddy, M. Hassan, V.G. Gomes, *Appl. Catal. A-Gen.* 489 (2015) 1–16.
- [28] H. Zhang, X.J. Lv, Y.M. Li, Y. Wang, J.H. Li, *ACS Nano* 4 (2010) 380–386.
- [29] S. Murgolo, F. Petronella, R. Ciannarella, R. Comparelli, A. Agostiano, M.L. Curri, G. Mascolo, *Catal. Today* 240 (Part A) (2015) 114–124.
- [30] M. Grandcolas, J. Ye, K. Miyazawa, *Ceram. Int.* 40 (2014) 1297–1302.
- [31] X.L. Yu, R.J. Liu, G.J. Zhang, H.B. Cao, *Nanotechnology* 24 (2013).
- [32] S.Y. Lim, W. Shen, Z.Q. Gao, *Chem. Soc. Rev.* 44 (2015) 362–381.
- [33] Y.Q. Zhang, D.K. Ma, Y.G. Zhang, W. Chen, S.M. Huang, *Nano Energy* 2 (2013) 545–552.
- [34] C.J. Liu, P. Zhang, F. Tian, W.C. Li, F. Li, W.G. Liu, *J. Mater. Chem.* 21 (2011) 13163–13167.
- [35] X.M. Li, M.C. Rui, J.Z. Song, Z.H. Shen, H.B. Zeng, *Adv. Funct. Mater.* 25 (2015) 4929–4947.
- [36] F. Karlicky, K.K.R. Datta, M. Otyepka, R. Zboril, *ACS Nano* 7 (2013) 6434–6464.
- [37] M. Zhang, L.L. Bai, W.H. Shang, W.J. Xie, H. Ma, Y.Y. Fu, D.C. Fang, H. Sun, L.Z. Fan, M. Han, C.M. Liu, S.H. Yang, *J. Mater. Chem.* 22 (2012) 7461–7467.
- [38] H. Peng, J. Travas-Sejdic, *Chem. Mater.* 21 (2009) 5563–5565.
- [39] Y.H. Yang, J.H. Cui, M.T. Zheng, C.F. Hu, S.Z. Tan, Y. Xiao, Q. Yang, Y.L. Liu, *Chem. Commun.* 48 (2012) 380–382.
- [40] Y.Q. Zhang, D.K. Ma, Y. Zhuang, X. Zhang, W. Chen, L.L. Hong, Q.X. Yan, K. Yu, S.M. Huang, *J. Mater. Chem.* 22 (2012) 16714–16718.
- [41] C.Z. Zhang, R. Hao, H.B. Liao, Y.L. Hou, *Nano Energy* 2 (2013) 88–97.
- [42] X.Y. Zhai, P. Zhang, C.J. Liu, T. Bai, W.C. Li, L.M. Dai, W.G. Liu, *Chem. Commun.* 48 (2012) 7955–7957.
- [43] H. Nie, M.J. Li, Q.S. Li, S.J. Liang, Y.Y. Tan, L. Sheng, W. Shi, S.X.A. Zhang, *Chem. Mater.* 26 (2014) 3104–3112.
- [44] F.Y. Zheng, Z.H. Wang, J. Chen, S.X. Li, *RSC Adv.* 4 (2014) 30605–30609.
- [45] J. Wang, M.M. Gao, G.W. Ho, *J. Mater. Chem. A* 2 (2014) 5703–5709.
- [46] Z.H. Ai, L.L. Zhu, S. Lee, L.Z. Zhang, *J. Hazard. Mater.* 192 (2011) 361–367.
- [47] G.H. Wang, L. Xu, J. Zhang, T.T. Yin, D.Y. Han, *Int. J. Photoenergy* (2012).
- [48] H.J. Yu, Y.F. Zhao, C. Zhou, L. Shang, Y. Peng, Y.H. Cao, L.Z. Wu, C.H. Tung, T.R. Zhang, *J. Mater. Chem. A* 2 (2014) 3344–3351.
- [49] J. Angelo, L. Andrade, A. Mendes, *Appl. Catal. A-Gen.* 484 (2014) 17–25.
- [50] D.L. Zhao, G.D. Sheng, C.L. Chen, X.K. Wang, *Appl. Catal. B-Environ.* 111 (2012) 303–308.
- [51] S. Yin, H. Yamaki, M. Komatsu, Q.W. Zhang, J.S. Wang, Q. Tang, F. Saito, T. Sato, *Solid State Sci.* 7 (2005) 1479–1485.
- [52] Y. Shu, H. Yamaki, Q.W. Zhang, M. Komatsu, J.S. Wang, T. Qing, F. Saito, T. Sato, *Solid State Ionics* 172 (2004) 205–209.
- [53] J.G. Yu, H.G. Yu, B. Cheng, M.H. Zhou, X.J. Zhao, *J. Mol. Catal. A-Chem.* 253 (2006) 112–118.
- [54] A. Mills, C. Hill, P.K.J. Robertson, *J. Photochem. Photobiol. A* 237 (2012) 7–23.
- [55] Z.H. Ai, W.K. Ho, S. Lee, *Appl. Surf. Sci.* 263 (2012) 266–272.
- [56] H. Ming, Z. Ma, Y. Liu, K.M. Pan, H. Yu, F. Wang, Z.H. Kang, *Dalton T.* 41 (2012) 9526–9531.